



# Ti<sub>3</sub>C<sub>2</sub>T<sub>x</sub> MXene/alginate-based electrodes for supercapacitors

Jorge Alexandre Alencar Fotius<sup>1,2</sup>, Murilo Henrique Moreira Facure<sup>3</sup>, Daniel Souza Correa<sup>4</sup>, Emanuel Carrilho<sup>3</sup>, Hernane da Silva Barud<sup>5</sup>, Helinando Pequeno de Oliveira<sup>1,a)</sup>

<sup>1</sup>Instituto de Pesquisa em Ciência dos Materiais, Universidade Federal do Vale do São Francisco, Juazeiro, BA 48902-300, Brazil

<sup>2</sup>Instituto Federal de Educação, Ciência e Tecnologia do Sertão Pernambucano, Petrolina, PE 56316-686, Brazil

<sup>3</sup>Instituto de Química de São Carlos, Universidade de São Paulo, São Carlos, SP 13566-590, Brazil

<sup>4</sup>Laboratório Nacional de Nanotecnologia Aplicada ao Agronegócio (LNNA), Embrapa Instrumentação, São Carlos, SP 13560-970, Brazil

<sup>5</sup>Laboratório de Biopolímeros e Biomateriais (BioPolMat), University of Araraquara, Araraquara, SP 14801-320, Brazil

<sup>a)</sup>Address all correspondence to this author. e-mail: helinando.oliveira@univasf.edu.br

Received: 24 January 2025; accepted: 22 April 2025

The promising application of MXenes in energy storage-based solutions is seriously affected by stacking processes that reduce available active sites for charge accumulation. Incorporating MXene into biopolymer templates represents a promising strategy to avoid aggregation of active electrochemical compounds, resulting in the optimization of the specific capacitance and energy/power density. Herein, the production of Ti<sub>3</sub>C<sub>2</sub>T<sub>x</sub>/alginate composites is explored as a part of a strategy to reduce the aggregation degree in MXene while preserving the electrical output performance of the overall electrode. By effectively incorporating MXene into sodium alginate-based electrodes, the energy density and power density of a 2-electrode device were 10.2 Wh kg<sup>-1</sup> and 1724.1 W kg<sup>-1</sup>, respectively. This paper highlights a competitive device prototype with a reduced MXene content compared to a pure MXene electrode, significantly lowering the final cost of the resulting supercapacitor due to the lower density of the active electrochemical filler.

## Introduction

The increasing demand for sustainable energy storage devices makes supercapacitors (SCs) a promising technology due to their outstanding high power density, fast charge–discharge cycles, and extended operational lifespan. Energy storage in SCs is based on Faradaic and non-Faradaic processes involving surface or interfacial phenomena (electrical double-layer capacitance—EDLC and pseudocapacitive—PC processes). In EDLC, energy is stored at the electrode and the electrolyte interface by the accumulation of ions. This non-Faradaic process enables rapid charge and discharge cycles, which results in devices with characteristic high power density [1]. In pseudocapacitive materials, energy storage occurs through Faradaic processes, such as reversible redox reactions, ion intercalation, or electrochemical adsorption at the electrode surface [1]. These processes allow for higher energy storage while maintaining the fast response time typical of EDLC systems [1, 2].

Conducting polymers, such as polyaniline (PANI) [3] and polypyrrole (PPy) [4], and transition metal oxides [5]

(manganese dioxide (MnO<sub>2</sub>) and ruthenium oxide (RuO<sub>2</sub>)) often exhibit pseudocapacitive behavior due to the energy storage mechanism based on surface redox reactions. Despite promising properties for EDLC and PC prototypes, the energy density of EDLC supercapacitors is lower than that of batteries. As an alternative, researchers have developed hybrid supercapacitors that integrate materials capable of promoting pseudocapacitive behavior to overcome this limitation [2, 6].

Recent breakthroughs in advanced materials have been observed using MXenes, showing both EDLC and pseudocapacitance mechanisms. Due to their unique properties, MXenes [1], a family of two-dimensional (2D) transition metal carbides, nitrides, and carbonitrides, have emerged as promising materials for supercapacitor applications [1, 7]. The layered structure of MXenes—composed of transition metals separated by carbon or nitrogen atoms—provides a high density of ion-accessible sites, facilitating both EDLC and pseudocapacitance mechanisms. Their superior conductivity ensures fast charge transfer, making them ideal for applications, such as electric vehicles,

portable electronics, and regenerative braking systems [7]. These processes enable MXenes to perform both storage mechanisms simultaneously, enhancing energy density without sacrificing power density output.

The outstanding capacity of MXene, particularly of titanium carbide ( $Ti_3C_2T_x$ ), is mainly related to its surface chemistry. During its synthesis, the MXene surface is usually modified with functional groups, such as hydroxyl (-OH), oxygen (=O), and fluorine (-F), represented by the  $T_x$  in the chemical formula, which enhances ion adsorption and promotes pseudocapacitive processes [8, 9]. Despite these advantages, MXenes tend to restack, limiting ion mobility and reducing the electrochemical performance of derived supercapacitors. The development of MXene-polymer composites has been explored to address this issue, preventing restacking and improving electrolyte penetration [1]. Polymers such as polyvinyl alcohol (PVA) enhance the mechanical stability of MXene electrodes, ensuring consistent performance over extended charge–discharge cycles [10, 11].

Alginate, a natural polymer derived from seaweed or synthesized by microorganisms (bacterial alginate), offers several advantages, including high ion exchange capacity, biocompatibility, and mechanical flexibility [12]. Alginate-based electrodes are suitable for wearable and biomedical devices due to their intrinsic flexibility and compatibility with biologic environments.

By combining alginate—whether derived from seaweed or microorganisms—with advanced materials, such as metal oxides or graphene, researchers aim to develop supercapacitors with high energy density, long cycle life, and enhanced performance for several applications [12, 13]. The combination of supports and active electrochemical components can provide structural integrity, consistent ion transport, and improved electrode performance throughout extended charge–discharge cycles. The controlled conditions for composites' preparation affect supercapacitor design and functionality. As reported in the literature, MXenes tend to restack during electrochemical measurements, which limits ion mobility and reduces electrolyte access to active sites [14]. Integrating MXenes with alginate can prevent restacking and improve electrolyte penetration throughout the electrode.

It is worth mentioning that promising applications involving alginate and MXene have been considered in the literature, ranging from environmental/biologic to energy-related areas, such as in the development of lead and copper ion removal assays [11], piezoresistive sensors [15], triboelectric nanogenerators [16], electromagnetic shielding devices [17, 18], solar energy conversion [19], self-healing-based devices [20], photothermal treatment [21], antibacterial agents [22], and supercapacitors [23]. In common, for all applications, the electroactive behavior and aggregation level of MXene are critical for improving the device's performance. Consequently, the adequate disposition of

the active layer into the composite critically affects the specific application.

Herein, the influence of alginate on the intercalation process of MXene in MXene-alginate compounds is evaluated as a part of a strategy to minimize the costs involved in the production of MXene-based supercapacitors with corresponding devices prepared with pure MXene. With this aim, a simple method for impregnating MXene into a sodium alginate matrix is reported to produce a 2-electrode symmetric supercapacitor, in which the content of MXene is reduced in the composite compared with a pure electrode under corresponding conditions for electrochemical performance. Due to the intercalation of the alginate into the MXene sheets, the restacking of the  $Ti_3C_2T_x$  layers is prevented, and consequently, the device's electrochemical performance is enhanced.

## Results and discussion

SEM images in Fig. 1 were explored to elucidate the characteristic morphology of  $Ti_3C_2T_x$  and  $Ti_3C_2T_x$ -Alg samples, displaying images of  $Ti_3C_2T_x$  particles and the cross-section of the  $Ti_3C_2T_x$ -Alg film, which is in agreement with results previously reported in the literature [24, 25]. MXene-based membranes are assembled by stacking the 2D structures with surfaces characterized by wrinkles and roughness (plicate feature). These features indicate partially exfoliated sheets, commonly resulting from the synthesis or etching process, which can introduce structural defects and influence the device's electrochemical response [26]. Figure 1(a) and (b) presents the top view of a  $Ti_3C_2T_x$  membrane, in which a roughness degree of stacked 2D structures can be visualized. For comparison, the SEM images for the cross-section of the  $Ti_3C_2T_x$ -Alg sample [shown in Fig. 1(c) and (d)] indicate the disposition of a less dense laminated structure of  $Ti_3C_2T_x$  intercalated by sodium alginate. This coexistence of wrinkles and flat regions plays a crucial role, as it ensures increased surface area for ion interactions and maintains pathways for efficient ion transport [27, 28].

The FTIR spectra [Fig. 2(a)] scrutinized the chemical structure of  $Ti_3C_2T_x$  (curve in black) and  $Ti_3C_2T_x$ -Alg (curve in red). The synthesis process involving HF (hydrofluoric acid), HCl (hydrochloric acid), and LiCl (lithium chloride) promotes the etching and exfoliation of MXene layers, increasing the surface area and providing interactions with alginate. In the spectrum of MXene, the broad peak near  $3450\text{ cm}^{-1}$  corresponds to O–H stretching, indicating the presence of hydroxyl groups. The peak at  $1620\text{ cm}^{-1}$  reflects O–H bending, suggesting surface-bound water or hydroxyl groups. Peaks between  $1200\text{ cm}^{-1}$  and  $1000\text{ cm}^{-1}$  represent C–F stretching, confirming the presence of fluorinated groups from synthesis. A peak near  $550\text{ cm}^{-1}$  corresponds to Ti–O stretching, demonstrating that the integrity of the titanium layer is maintained [29, 30].

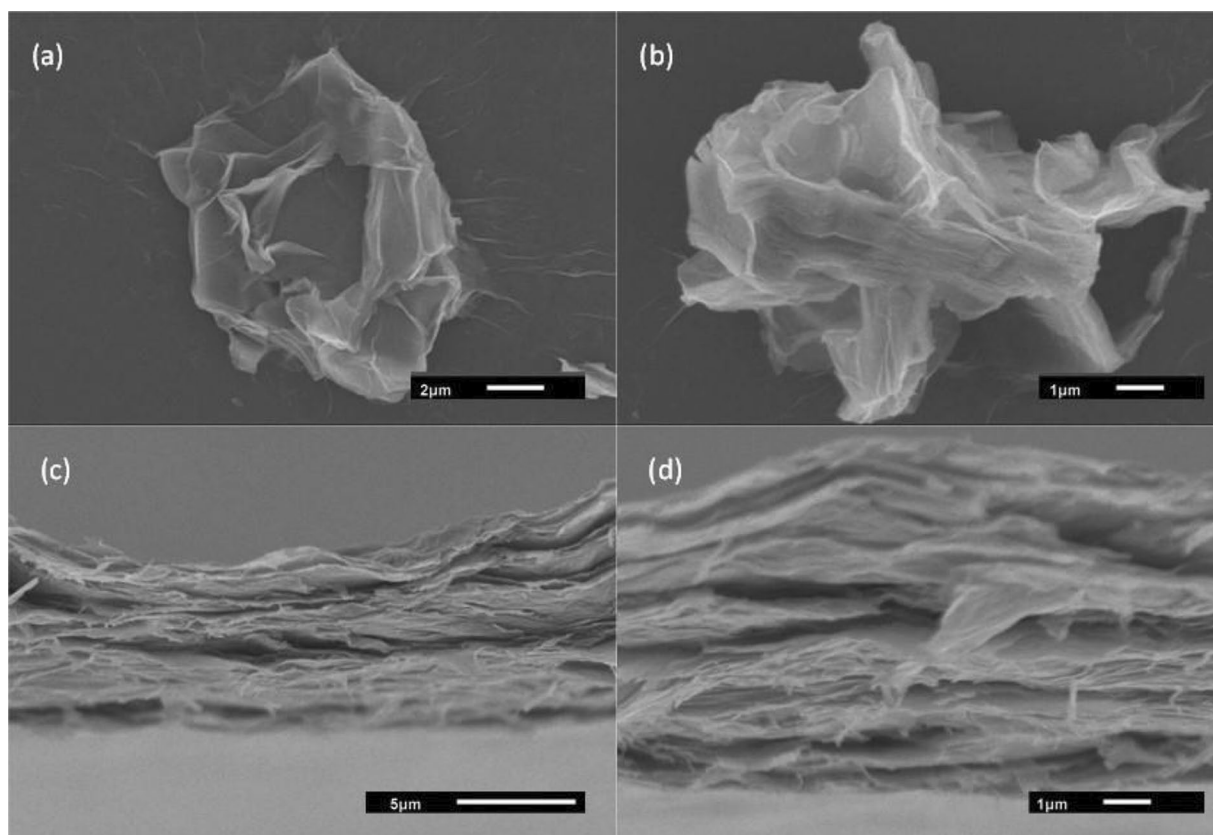


**Figure 1:** Top ((a) and (b)) and cross-sectional-view ((c) and (d)) from SEM images of  $\text{Ti}_3\text{C}_2\text{T}_x$  and  $\text{Ti}_3\text{C}_2\text{T}_x\text{-Alg}$  films, respectively, indicating the influence of the intercalation of sodium alginate on laminated MXene.

The  $\text{Ti}_3\text{C}_2\text{T}_x\text{-Alg}$  composite spectrum shows significant shifts in the peak position, indicating chemical interactions between the materials due to aliphatic C–H stretching, reflecting the presence of organic backbones at approximately  $3000\text{ cm}^{-1}$  [30]. A pronounced peak at  $1620\text{ cm}^{-1}$  corresponds to C=O stretching from alginate's carboxyl groups. Peaks near  $1400\text{ cm}^{-1}$  correspond to C–H bending and RCO–O stretching, confirming further structural modifications. The persistence of peaks between  $1000\text{ cm}^{-1}$  and  $1200\text{ cm}^{-1}$  confirms the presence of residual fluorine groups, while the Ti–O peak at  $550\text{ cm}^{-1}$  indicates that MXene's structure remains intact [29]. These findings demonstrate that the MXene and alginate interact efficiently to form the final composite [11, 16, 31].

The X-ray diffraction patterns shown in Fig. 2(b) confirm the structural transformation from  $\text{Ti}_3\text{AlC}_2$  to  $\text{Ti}_3\text{C}_2\text{T}_x$  and further to the  $\text{Ti}_3\text{C}_2\text{T}_x\text{-Alginate}$  composite. The reference pattern of the MAX phase  $\text{Ti}_3\text{AlC}_2$ , obtained from the ICSD card no. 153266 is shown in blue and serves as a structural baseline for comparison. After selective etching, the  $\text{Ti}_3\text{C}_2\text{T}_x$  sample (red curve) exhibits a broad (002) peak centered at  $\sim 9.48^\circ$ , corresponding to a  $d(002)$  spacing of  $9.32\text{ \AA}$ , indicative of partial delamination and reduced stacking order. Upon intercalation with sodium alginate (black curve), this peak shifts to  $\sim 7.0^\circ$ ,

resulting in a  $d(002)$  of  $12.62\text{ \AA}$ , according to the method described in Refs. [32, 33], subtracting the theoretical thickness of a  $\text{Ti}_3\text{C}_2$  monolayer ( $4.605\text{ \AA}$ ) gives interlayer spacings of  $4.72\text{ \AA}$  and  $8.01\text{ \AA}$  for  $\text{Ti}_3\text{C}_2\text{T}_x$  and  $\text{Ti}_3\text{C}_2\text{T}_x\text{-Alg}$ , respectively. The increase in spacing reflects the successful intercalation of alginate chains between the MXene layers, effectively preventing restacking and promoting an expanded lamellar structure. Such shifts in the (002) reflection are characteristic of structural reorganization in 2D MXenes, in which selective etching removes Al atoms from the MAX phase and leads to layered carbides with surface terminations (–O, –F, –OH) [34, 35]. The resulting electrostatic repulsion and hydration effects can facilitate spontaneous interlayer expansion. In particular, sodium ions and polar functional groups of alginate enhance interfacial interactions. It enables polymer intercalation, as previously observed for systems incorporating DMSO [36], sodium alginate [37], or PVA [38]. The structural modification observed in the  $\text{Ti}_3\text{C}_2\text{T}_x\text{-Alg}$  sample also leads to greater accessibility for ion diffusion and electrochemical reactions. Increased interlayer distances improve ion mobility, enhance charge storage, and stabilize the layered architecture against collapse during cycling. Furthermore, DFT studies have shown that expanded interlayer spacing reduces migration barriers and enables co-intercalation

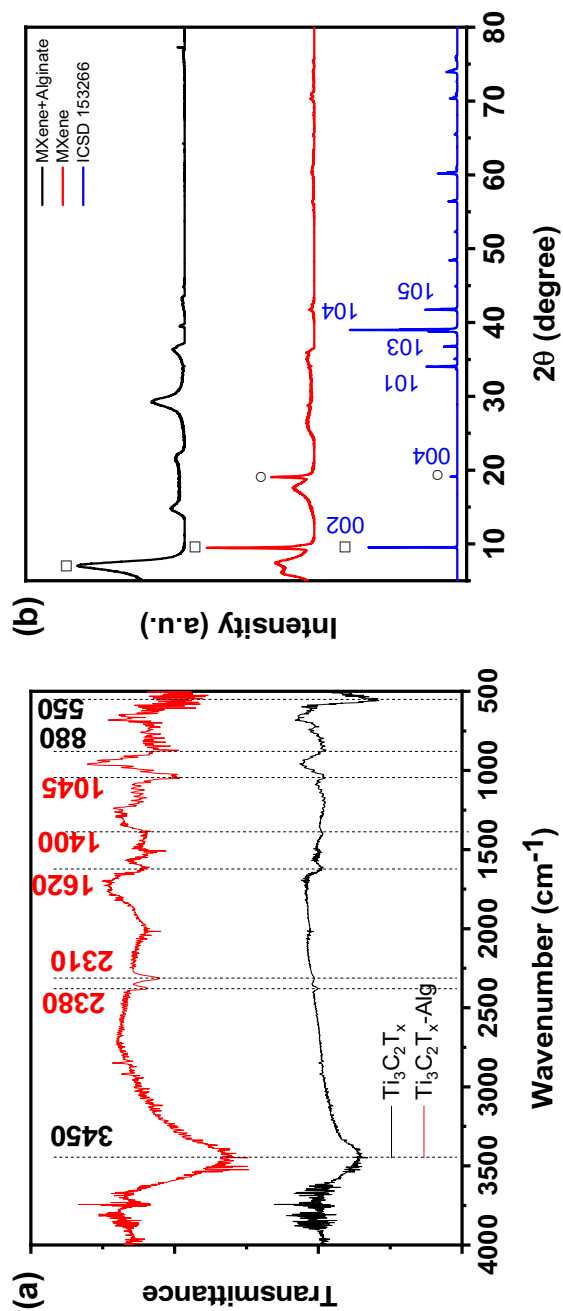


**Figure 2:** Spectroscopic characterizations of the MXenes in (a) FTIR spectra of pristine  $Ti_3C_2T_x$  (curve in black) and  $Ti_3C_2T_x$ -Alg (curve in red), showing characteristic peaks of O-H, C-F, and Ti-O, with additional alginate-related bands and (b) XRD patterns highlighting structural changes from  $Ti_3AlC_2$  to  $Ti_3C_2T_x$  (curve in red) and  $Ti_3C_2T_x$ -Alg (curve in black), including peak shifts and interlayer expansion. The blue curve represents the XRD pattern of the  $Ti_3AlC_2$  (ICSD 153266).

of solvated ions, reinforcing the benefits of hybrid architectures for energy storage [33].

The electrochemical performance of the symmetric 2D supercapacitors assembled with electrodes of  $Ti_3C_2T_x$  and  $Ti_3C_2T_x$ -Alg was initially evaluated by the cyclic voltammetry (CV) assays at different scan rates [Figs. 3(a) and 4(b)]. It is

worth noting that different aspects must be considered from CV curves (enclosed area and format of curves). Initially, a general dependence on the current value is observed at increasing scan rate. As reported in the literature, [3, 39–43], the diffusion layer will grow much more from the electrode at a slow scan rate than at a fast scan rate. This inverse relationship of

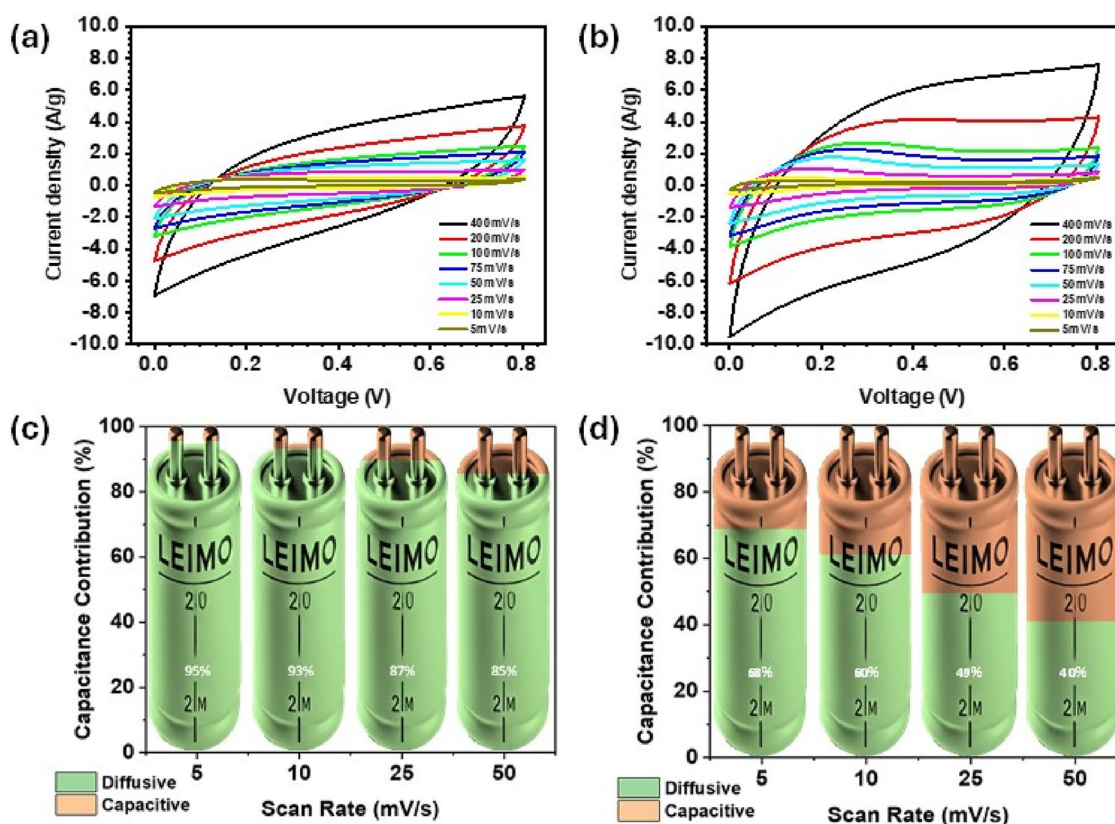


**Figure 3:** Cyclic voltammetry (CV) curves of  $Ti_3C_2T_x$  (a) and  $Ti_3C_2T_x$ -Alg (b) at varying scan rates in the range of 5 mV/s to 400 mV/s. The corresponding distribution of diffusive and capacitive terms in the overall response of CV curves for  $Ti_3C_2T_x$  (c) and  $Ti_3C_2T_x$ -Alg (d).

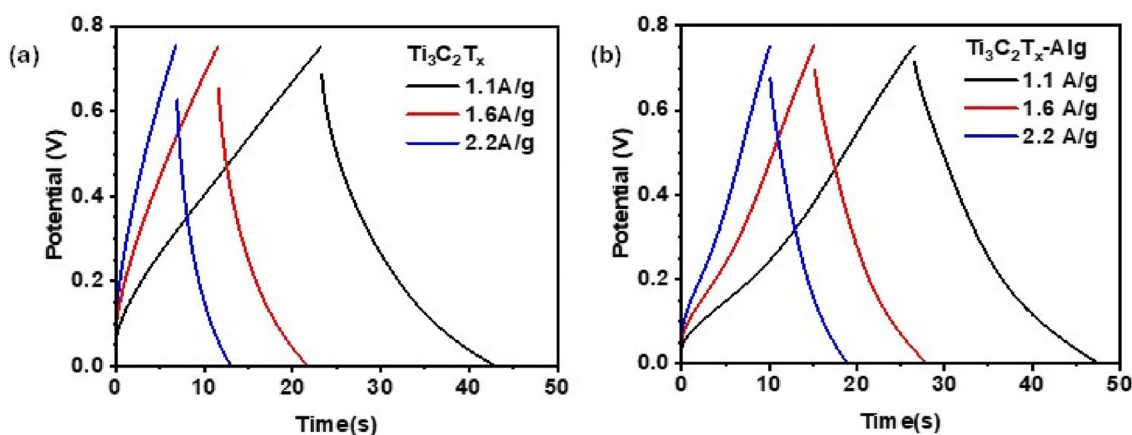


**Figure 4:** Galvanostatic charge–discharge (GCD) curves for  $Ti_3C_2T_x$  (a) and  $Ti_3C_2T_x$ -Alg (b), confirming the best electrochemical performance for  $Ti_3C_2T_x$ -Alg regarding the longer charge–discharge time in comparison with the pure  $Ti_3C_2T_x$ .

dependence (thinner diffusion layer at a faster scan rate) facilitates the flux of counterions to the electrode surface and, consequently, the resulting current. As shown in Fig. 3(a) and (b), current enhances with increasing scan rate, which agrees with the previously reported behavior, with higher current values (measured at the same voltage and scan rate) observed for sample  $\text{Ti}_3\text{C}_2\text{T}_x\text{-Alg}$ .

Another critical aspect is the CV diagram format at an increasing scan rate. As observed, the curves migrate from a square shape to distortions (prolate format) at a faster scan rate for both samples. As reported in the literature, rectangular-shaped curves in CV diagrams confirm the prevailing EDLC behavior in overall response, while the slight distortion has been attributed to the pseudocapacitive behavior [3, 39–41]. The change in the format of the CV curve is a consequence of the difference in electrolyte resistance in the bulk/surface of the electrode. Consequently, a significant distortion in the format of CV curves is expected under increasing resistance inside the compact layers of the stacked material.

In terms of curve shape, as observed in Fig. 3(a) and (b), there is a general change from a quasi-squared shape at a low scan rate (prevailing EDLC behavior at thicker diffusion layer) to a prolate curve at a faster scan rate in which the thinner diffusion layer favors the PC mechanisms into stacked structures of  $\text{Ti}_3\text{C}_2\text{T}_x$  or a more intercalated structure of  $\text{Ti}_3\text{C}_2\text{T}_x\text{-Alg}$ .

The evaluation of the distribution degree between diffusive and capacitive terms in both experimental systems makes use of Eq. 1 [2, 44]:

$$i(V) = k_1 v + k_2 \sqrt{v}, \quad (1)$$

where  $k_1 v$  represents the capacitive contribution, proportional to the scan rate ( $v$ ) and  $k_2 \sqrt{v}$  corresponds to the diffusion-controlled contribution, which scales with the square root of the scan rate ( $\sqrt{v}$ ). By analyzing the dependence of current on scan rate,  $k_1$  and  $k_2$  can be extracted, providing insight into the underlying electrochemical mechanisms and the relative contributions of surface and bulk processes to the total capacitance.

Figure 3(c) and (d) summarizes each sample's relative diffusive/capacitive terms contribution. As expected, the diffusive behavior prevails at lower scan rate values for both experimental systems, while the capacitive behavior is favored at a faster scan rate regime.

Regarding the balance between contributions, the results for the  $\text{Ti}_3\text{C}_2\text{T}_x$  system indicate that diffusion-controlled mechanisms predominantly govern charge storage in pure MXene. By increasing the scan rate from 5 to 50  $\text{mVs}^{-1}$ , there is a decrease in the contribution of the diffusion-controlled process from 95 to 85%, indicating that ion transport within the layered MXene structure is still favored as a dominant process for charge accumulation. On the other hand, the response for the  $\text{Ti}_3\text{C}_2\text{T}_x\text{-Alg}$  composite revealed a significant shift in the charge storage

mechanism. The capacitive contribution rises from 32 to 60% as the scan rate increases from 5 to 50  $\text{mV/s}$ , while the diffusion-controlled contribution decreases from 68 to 40%. This change implies that the incorporation of alginate enhances ion accessibility and surface interactions, potentially by increasing porosity or creating a more open structure that facilitates ion diffusion [45–47].

As an alternative to determining the electrochemical performance of supercapacitors by CV curves, galvanostatic charge–discharge (GCD) assays provide corresponding information regarding the current density, which is an important factor in the electrochemical robustness of the device. Figure 4(a) and (b) show the GCD curves for both  $\text{Ti}_3\text{C}_2\text{T}_x$  and  $\text{Ti}_3\text{C}_2\text{T}_x\text{-Alg}$  films applied in 2-electrode SCs. The general behavior of a longer charge–discharge time at decreasing current density is observed for both curves. Another critical aspect to be considered is the lower IR drop observed at a current density as high as 2 A/g, indicating a lower internal resistance for both devices. From a direct comparison of the performance of the devices, a longer discharge time is observed for  $\text{Ti}_3\text{C}_2\text{T}_x\text{-Alg}$ -based SC, indicating the promising effects of the intercalation provided by sodium alginate.

Applying Eqs. 2 and 3 quantifies the specific (gravimetric and areal) capacitance versus scan rate and current density. The results shown in Fig. 5(a) ( $\text{Ti}_3\text{C}_2\text{T}_x$ ) and 5(b) ( $\text{Ti}_3\text{C}_2\text{T}_x\text{-Alg}$ ) confirm that, as expected, the specific capacitance tends to be reduced at increasing scan rates. This process has been justified by the time-dependent behavior of material that provides a limited density of available sites for charge accumulation under a specific time for occupation. Under increasing scan rates, fewer accessible sites are available for the diffusive species and the following charge accumulation step. As can be noted, higher values for specific capacitance at lower scan rates are observed for  $\text{Ti}_3\text{C}_2\text{T}_x\text{-Alg}$ , which is associated with the lowest variation in the corresponding scan rate window, characterizing a more stable performance in the complete range of variation in the external excitation. In correspondence, the calculated value for specific capacitance from GCD data [see Fig. 5(c)] confirms that the gravimetric capacitance of the  $\text{Ti}_3\text{C}_2\text{T}_x\text{-Alg}$ -based supercapacitor is minimally affected by current density, presenting a minimal variation in the excursion of the external current of charge. Corresponding values for areal capacitance are shown on the right side of Fig. 5(a), (b), and (c). These results suggest that adding alginate may have improved structural stability and ion transport under fast charge/discharge conditions [20].

The performance of MXene-based SCs directly depends on the impedance of the resulting material. Nyquist plots in Fig. 6(a) and (b) present a semi-circular portion at high frequencies, followed by a linear tail at low frequencies, indicating a combination of charge transfer and diffusion processes.

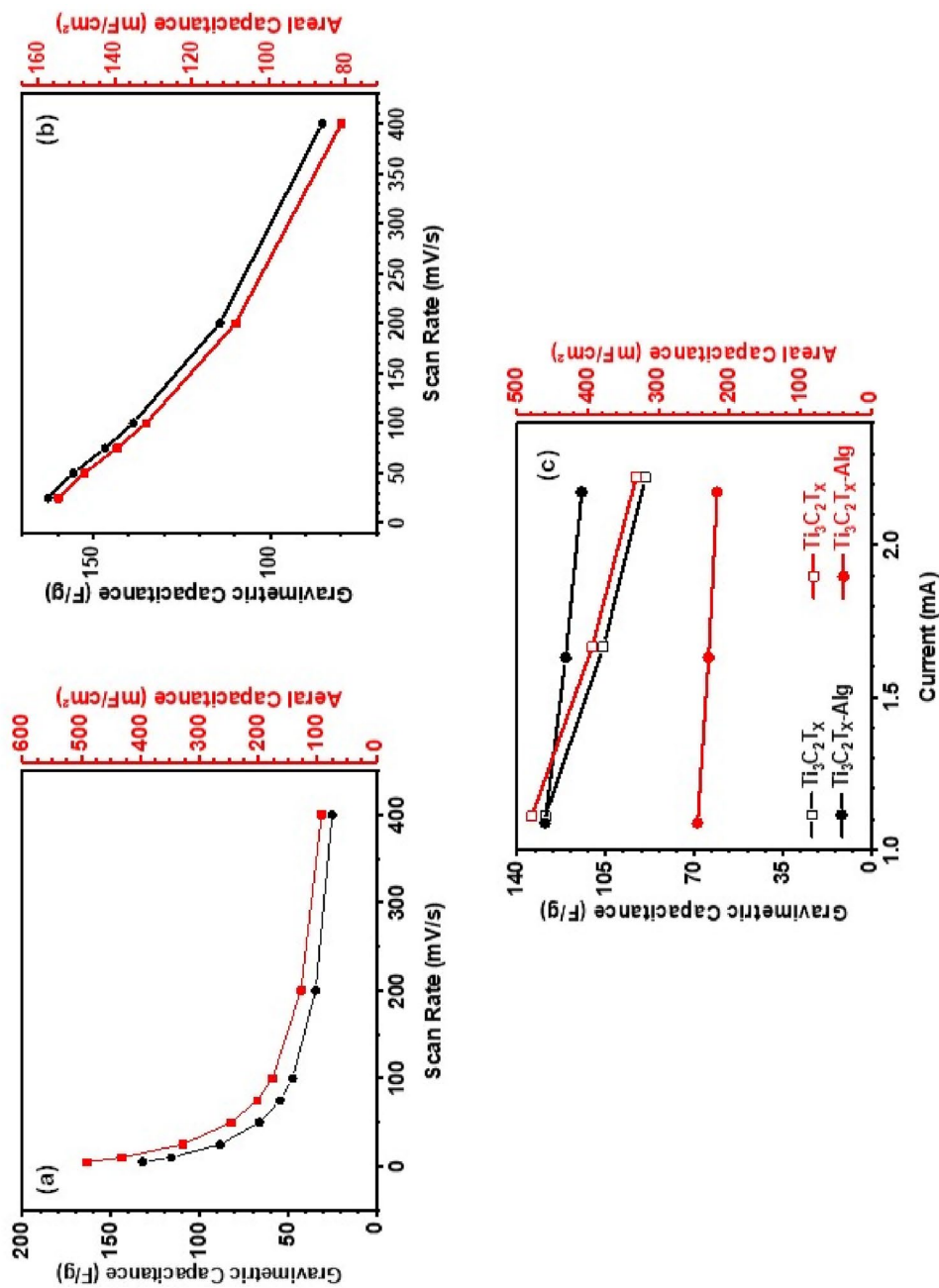


Figure 5: Comparison of electrochemical performance (gravimetric (curves in black) and areal (curves in red)) for  $Ti_3C_2T_x$  (a) and  $Ti_3C_2T_x-Alg$  (b) as a function of scan rate and both samples as a function of the current (c).

Regarding the response of  $Ti_3C_2T_x$  in Fig. 6(a), the close fit between the experimental data and the circuit model suggests that the chosen model accurately captures the impedance behavior of the system—the solution resistance ( $R_{sol}$ ) of  $0.370 \Omega$  is coherent with its known high ionic conductivity [48, 49]. The double-layer capacitance ( $C_{dl}$ ) of  $32.253 \text{ mF}$  suggests substantial charge storage at the interface between MXene and the electrolyte. The charge transfer resistance ( $R_{ct}$ ) of  $0.083 \Omega$  indicates efficient electron transfer, a typical property of MXene due to its high electrical conductivity [50]. The value of  $C_{pe}$  ( $0.264 \text{ mF}$ ) reflects the pseudocapacitive behavior contributing to overall capacitance by facilitating faradaic reactions. This combination of double-layer and pseudocapacitive mechanisms enhances the energy storage capabilities of the supercapacitor beyond those of traditional capacitors [28]. The Warburg impedance ( $Z_w$ ), characterized by  $T_{dif} = 3.769 \text{ ms}$  and  $R_{dif} = 0.346 \Omega$ , highlights the finite ion diffusion within the porous MXene structure, influencing the discharge rate and the overall power performance [51].

Regarding the fitting data in Fig. 6(b) for  $Ti_3C_2T_x$ -Alg, the Nyquist plot features a semi-circular region at high frequencies transitioning into a steeply inclined line at lower frequencies, which is indicative of significant charge transfer resistance and a diffusion-controlled process. The circuit model fitting to the data (red line) closely matches the experimental points (black), suggesting that the model accurately represents the system's impedance characteristics. The solution resistance ( $R_{sol}$ ) is  $0.329 \Omega$ , demonstrating good ionic conductivity within the electrolyte. The double-layer capacitance ( $C_{dl}$ ) is  $156.18 \text{ mF}$ , implying substantial charge storage capability at the electrode–electrolyte interface. This enhanced capacitance may be attributed to the synergistic effect of MXene's high surface area combined with alginate's stabilizing and conductive properties, improving ion

distribution. A significant finding is the charge transfer resistance ( $R_{ct}$ ) of  $75.74 \Omega$ , higher than typical values for pure MXene. This increase suggests that while alginate supports ionic transport and structural integrity, it might introduce additional resistance due to forming a matrix that impacts electron mobility. The Warburg impedance ( $Z_w$ ), with a time constant ( $T_{dif}$ ) of  $783.53 \text{ ms}$  and a diffusion resistance ( $R_{dif}$ ) of  $4.642 \Omega$ , indicates a more restricted ion diffusion process.

In addition to the electrical characterization using CV, GCD curves, Nyquist plots, and corresponding determination of the specific capacitance, additional parameters must be considered, such as the retention of electrochemical performance under use and the resulting power/energy density. Regarding the Ragone plot combined with the potential window [see Fig. 7(a)], both materials' energy and power densities are compared with the corresponding data reported in the literature. The Ragone plot for  $Ti_3C_2T_x$  [see Fig. 7(a)] displays a moderate specific energy density at lower power densities but shows a pronounced decline in energy density as the power density increases [52]. Such behavior is characteristic of conventional supercapacitors that favor rapid charging and discharging cycles [11, 53]. In contrast, the Ragone plot for  $Ti_3C_2T_x$ -Alg in Fig. 7(a) illustrates higher power density while maintaining competitive energy density, demonstrating that adding alginate enhances the supercapacitor's capability for power delivery without drastically impacting energy density. The alginate likely provides structural support and improves ionic conductivity, improving performance under high-power operations. The composite's performance surpasses that of MXene alone in terms of power density, making it suitable for applications that require rapid energy release [28, 51]. A conventional 2D Ragone plot is provided in Fig. 7(b) for direct comparison.

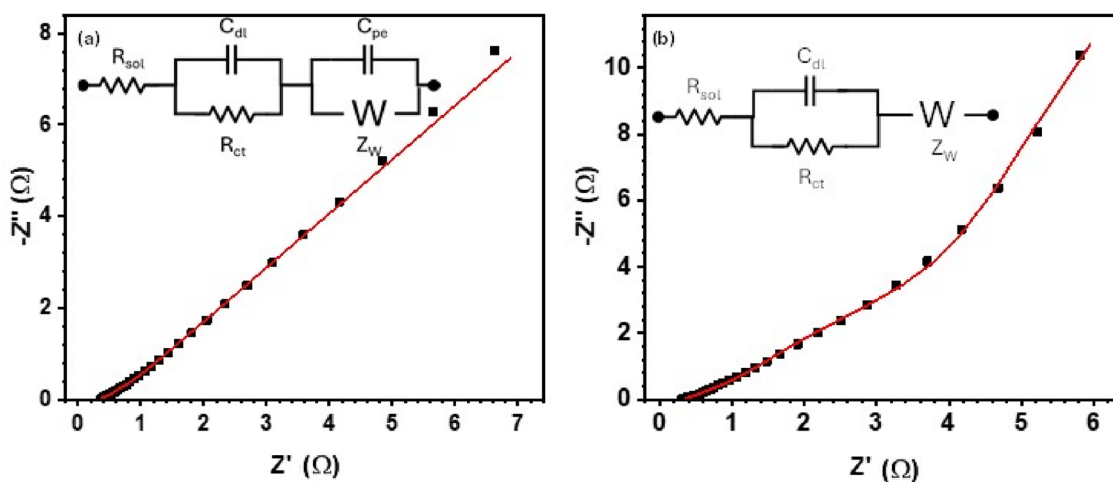


**Figure 6:** Nyquist plot for  $Ti_3C_2T_x$  (a) and  $Ti_3C_2T_x$ -Alg (b) with the corresponding equivalent circuit (inset) and fitting plot (curve in red) characterizing low values for solution resistance and general behavior of prevailing diffusive mechanisms, represented by Warburg element.

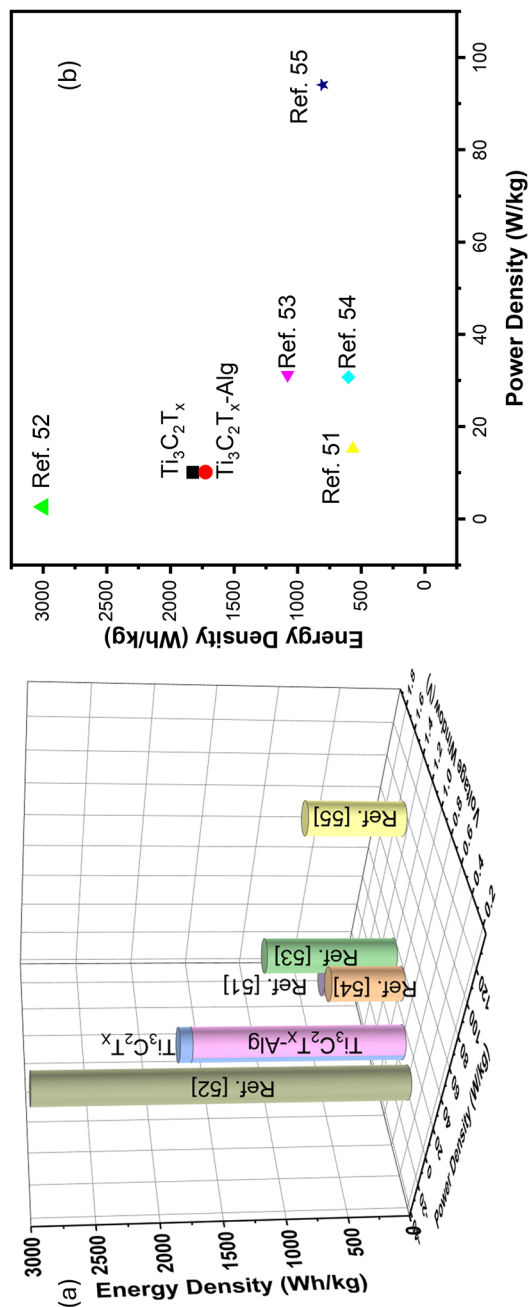


Figure 7: Supercapacitor characterization of MXenes in (a) 3D map for energy density vs. power density and (b) the Ragone plot comparing the energy and power density of  $Ti_3C_2T_x$  and  $Ti_3C_2T_x$ -Alg supercapacitors with systems reported in the literature.

For comparison, Table 1 provides the corresponding experimental conditions and values of specific capacitance, energy density, and power density, confirming the competitive values for energy density and power density of  $Ti_3C_2T_x$  and  $Ti_3C_2T_x$ -Alg that require a lower density of active material (MXene) by the adequate intercalation of their platelets into the polymeric matrix. As can be seen, a wide range of variation in the energy density in the range of 2 – 94 Wh kg<sup>-1</sup> and power density from 200 to 8500 W kg<sup>-1</sup> is observed for MXene-based compounds. These results reinforce the relevance of the development of bio-based composites for MXene-based solutions in energy since they result in economic advantages (low content of active electrochemical material) and an adequate morphology that avoids the MXene stacking process.

In terms of the retention of the electrochemical performance under successive use of devices, Fig. 8(a) and (b) summarizes the capacitive retention and coulombic efficiency after 3,000 cycles of charge/discharge at high current density (3 A/g). Regarding discharge current retention [Fig. 8(a)], pure  $Ti_3C_2T_x$  retains over 87.5% of their initial discharge current after 3000 cycles, reflecting their robust structural and electrochemical stability. On the other hand,  $Ti_3C_2T_x$ -Alg maintains approximately 80% of its discharge current by the 50th cycle, suggesting a reduction in cycling performance at the beginning of the use. A constant slope is observed due to the degradation that retains around 70.8% of the initial performance after 3000 complete use cycles.

Regarding the coulombic efficiency, pure MXene consistently stabilizes around 76–77% throughout the cycling, indicating efficient charge–discharge reversibility. In contrast, the  $Ti_3C_2T_x$ -Alg system exhibits significantly higher coulombic efficiencies, consistently near 100%, showcasing excellent charge–discharge reversibility.

## Conclusion

The intercalation provided by alginate on MXene in membranes for supercapacitor electrodes mitigates the restacking issues inherent to MXene and enhances ion accessibility to ion diffusion and separation. The improved structural integrity of the MXene-alginate films contributes to a consistent performance due to the adequate combination of the electrochemical advantages of MXene’s high conductivity with the structural benefits of alginate. The pure MXene electrodes demonstrated higher gravimetric capacitance at low scan rates. Still, a decline was observed as the scan rate increased, reflecting limitations in ion transport (due to the variations in the diffusion layer). In contrast, the  $Ti_3C_2T_x$ -Alg composite maintained a more consistent performance, with the capacitive contribution rising from 32 to 60% as the scan rate increased, indicating that the alginate enhanced ion accessibility and surface-controlled storage

mechanisms. Also, the  $Ti_3C_2T_x$ -Alg composite showed more stable behavior at high scan rates and current density, suggesting alginate supports rapid ion transport. This enhancement is particularly relevant for applications requiring swift energy delivery.

Regarding energy density, the Ragone plot revealed that the MXene composite, while showing moderate specific energy at low power densities, experienced a notable decline as the current density increased. Conversely, the  $Ti_3C_2T_x$ -Alg composite demonstrated improved power density while maintaining competitive energy density, suggesting that alginate contributes to better structural support and ionic pathways. These findings emphasize the potential of MXene/alginate composites as a strategy to reduce resistance and enhance performance, leading to more efficient supercapacitor designs.

## Methodology

### Materials

$Ti_3AlC_2$  MAX phase and the alginic acid sodium salt from brown algae (Sigma-Aldrich), hydrochloric acid (HCl, 36%, Synth), and hydrofluoric acid (HF, 40%, Vetec) were used in the

MAX phase etching. Lithium chloride (LiCl, Synth) was used in the MXene delamination.

### $Ti_3C_2T_x$ synthesis (sample $Ti_3C_2T_x$ )

The MXene synthesis was performed as reported previously [68]. Briefly, 18 mL of HCl and 3.6 mL of HF were added to 8.4 mL of water in a poly(tetrafluoroethylene) container. Next, 1.5 g of the  $Ti_3AlC_2$  MAX phase was slowly added to the solution. The etching of the Al layer was performed for 24 h at 35 °C. The multilayer MXene was obtained by centrifugation of the mixture (3500 rpm for 5 min), which was performed until the pH of the dispersed supernatant was higher than 6. The delamination was performed by dispersing the obtained slurry in 75 mL of LiCl (0.5 mol/L), which was kept under stirring for 20 h. Centrifugation steps (3500 rpm for 5 min) were used to discard the LiCl and to collect the delaminated  $Ti_3C_2T_x$  when the supernatant started to present a black color. In the preparation of the MXene films, the  $Ti_3C_2T_x$  dispersion was concentrated by centrifuging it at 8000 rpm for 10 min and redispersing

**TABLE 1:** Comparison between the electrochemical performance of devices (energy density and power density) and constitutive aspects (electrolyte and concentration) reported in the literature and this work.

Electrode material	Voltage window	Electrolyte	Specific capacitance	Energy density	Power density	Refs
$Ti_3C_2T_x$ ionogel film	3 V	EMI-TFSI	62 F g <sup>-1</sup>	–	–	54
Pure MXene	0.8 V	1 M H <sub>2</sub> SO <sub>4</sub>	290 F g <sup>-1</sup> at 1 A g <sup>-1</sup>	–	–	55
MXene/CNT-5%	0.8 V	1 M H <sub>2</sub> SO <sub>4</sub>	300 F g <sup>-1</sup> at 1 A g <sup>-1</sup>	–	–	55
Ti <sub>2</sub> VC <sub>2</sub> film	0.6 V	1 M H <sub>2</sub> SO <sub>4</sub>	518 F g <sup>-1</sup> at 2 mV s <sup>-1</sup>	2.6 Wh kg <sup>-1</sup>	3000 W kg <sup>-1</sup>	56
3D networked MXene thin film	0.8 V	0.5 M H <sub>2</sub> SO <sub>4</sub>	100 F g <sup>-1</sup> at 5 mV s <sup>-1</sup>	8.8 Wh kg <sup>-1</sup>	0.2 kW kg <sup>-1</sup>	28
N- $Ti_3C_2T_x$ -MXene//Zn	1 V	1 M ZnSO <sub>4</sub>	582.96 F g <sup>-1</sup> at 1 A g <sup>-1</sup>	30.7 Wh kg <sup>-1</sup>	600.5 W kg <sup>-1</sup>	57
$Ti_3C_2T_x$ MXene/polyaniline composite films	1.2 V	1 M H <sub>2</sub> SO <sub>4</sub>	352.9 F g <sup>-1</sup> at 10 mV s <sup>-1</sup>	31.18 Wh kg <sup>-1</sup>	1079.3 W kg <sup>-1</sup>	58
Bismuth oxychloride nanosheet-immobilized $Ti_3C_2T_x$ MXene material (TCBOC)	1.2 V	1 M KOH	247.8 F g <sup>-1</sup>	15.2 Wh kg <sup>-1</sup>	567.4 W kg <sup>-1</sup>	59
Fe <sub>1</sub> Ni <sub>3</sub> -LDH/ $Ti_3C_2T_x$ -MXene	1.5 V	6 M KOH	301 F g <sup>-1</sup> at 1 A g <sup>-1</sup>	94.1 Wh kg <sup>-1</sup>	802.4 W kg <sup>-1</sup>	60
NiCo <sub>2</sub> S <sub>4</sub> /MXene//AC	1.7 V	3 M KOH	171.2 of 1 A g <sup>-1</sup>	34.0 Wh kg <sup>-1</sup>	8.5 kW kg <sup>-1</sup>	61
PPy/MXene/PMFF textiles electrodes	0.8 V	PVA/Na <sub>2</sub> SO <sub>4</sub> gel electrolyte	1295 mF cm <sup>2</sup> at 1 mA cm <sup>2</sup>	40.7 μW h cm <sup>2</sup>	0.5 mW cm <sup>2</sup>	62
MXene//AC-Nafion	2 V	3 M H <sub>2</sub> SO <sub>4</sub>	555 F.g <sup>-1</sup> at 1 A.g <sup>-1</sup>	81.2 Wh.kg <sup>-1</sup>	1023 W.kg <sup>-1</sup>	63
2D MXene/NiCoP + ZIF-derived porous carbon	1.6 V	2 M KOH (aqueous)	1754.0 F.g <sup>-1</sup> at 3 mA cm <sup>-2</sup>	54.3 Wh.kg <sup>-1</sup>	565.6 W.kg <sup>-1</sup>	64
N-doped $Ti_3C_2T_x$ (UN- $Ti_3C_2T_x$ )	2.4 V	1 M EMIMTFSI/LiTFSI in ACN	147 F.g <sup>-1</sup> at 0.5 A.g <sup>-1</sup>	29.4 Wh.kg <sup>-1</sup>	600 W.kg <sup>-1</sup>	65
CDP-MX/PA (PANI/MXene + cyclodextrin polymer)	1.4 V	1 M H <sub>2</sub> SO <sub>4</sub>	523.8 F g <sup>-1</sup> at 1 A g <sup>-1</sup>	27.7 Wh kg <sup>-1</sup>	700 W kg <sup>-1</sup>	66
PLA/PANI/MXene (PPM) Composite	0.6 V	1 M PVA/H <sub>2</sub> SO <sub>4</sub> gel	193.7 F g <sup>-1</sup> at 0.25 A g <sup>-1</sup>	9.3 Wh kg <sup>-1</sup>	291.3W kg <sup>-1</sup>	67
$Ti_3C_2T_x$	0.8 V	1 M H <sub>2</sub> SO <sub>4</sub>	128.9 F g <sup>-1</sup> at 1 A g <sup>-1</sup>	10.1 Wh kg <sup>-1</sup>	1824.8 W kg <sup>-1</sup>	This Work
$Ti_3C_2T_x$ -Alg	0.8 V	1 M H <sub>2</sub> SO <sub>4</sub>	129.1 F g <sup>-1</sup> at 1 A g <sup>-1</sup>	10.2 Wh kg <sup>-1</sup>	1724.1 W kg <sup>-1</sup>	This Work

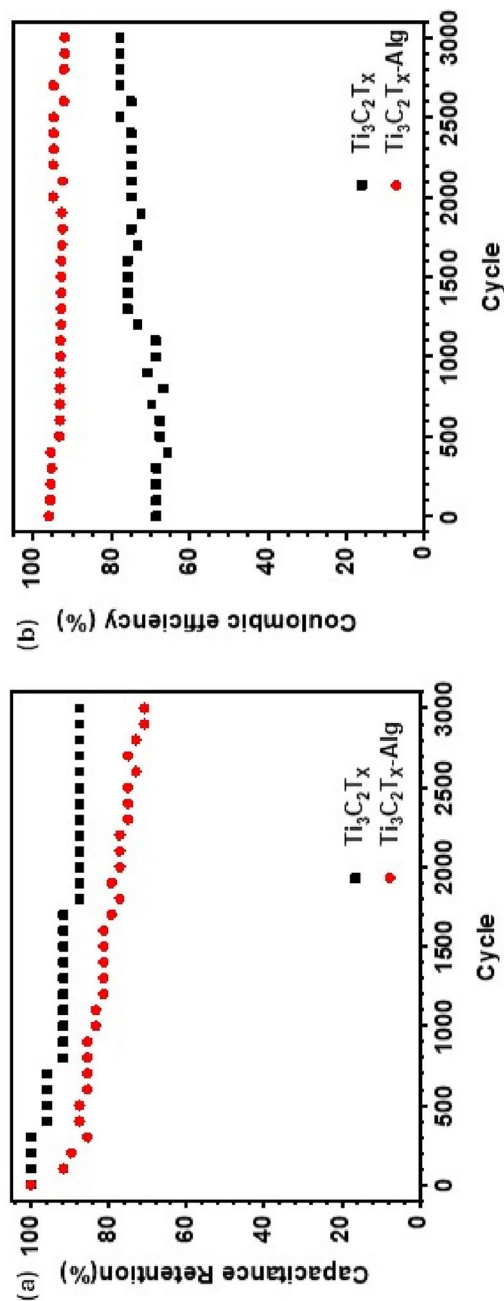


Figure 8: Electrochemical performance as (a) Capacitance retention and (b) Coulombic efficiency for  $Ti_3C_2T_x$  (black) and  $Ti_3C_2T_x$ -Alg (red) under a current density of 3 A/g.

the pellet [the schematic preparation of films of MXene is shown in Fig. 9(a)].

### $Ti_3C_2T_x$ /Alginate film preparation (sample $Ti_3C_2T_x$ -Alg)

The preparation of the MXene/alginate films involved dispersion of 1% (w/w) alginate solution and a 3.3-mg/mL  $Ti_3C_2T_x$  prepared using double-distilled water. From the stock solutions, a dispersion containing 100 mg of alginate and 100 mg of MXene was obtained and sonicated in an ultrasound bath for 5 min. Then, the dispersion was drop-cast over a glass covered with biaxially oriented polypropylene (BOPP) and left to dry at 35 °C overnight [the schematic preparation of sample  $Ti_3C_2T_x$ -Alg is shown in Fig. 9(b)].

### Supercapacitor assembly

The electrodes were cut into 1 cm squares and their masses were carefully measured (sample  $Ti_3C_2T_x$  and  $Ti_3C_2T_x$ -Alg). The mass density for  $Ti_3C_2T_x$  films was 7.4 mg cm<sup>-2</sup>, while 3.8 mg cm<sup>-2</sup> was the mass density for  $Ti_3C_2T_x$ -Alg electrodes. A standard filter paper was immersed in 1M H<sub>2</sub>SO<sub>4</sub> aqueous electrolyte and used as a separator. The supercapacitor devices were assembled by sandwiching the electrolyte-soaked separator between two identical electrodes of the same material.

### Materials characterization

The scanning electron microscopy (SEM) images were obtained using a JEOL 6510. The samples were prepared by drop-casting the  $Ti_3C_2T_x$  aqueous dispersion onto a silicon substrate and using a fractured  $Ti_3C_2T_x$ -Alg film. The structural components of the materials were analyzed through Fourier transform infrared spectroscopy (FTIR) using a Shimadzu IR-Prestige 21 spectrometer. For these measurements, pellets were prepared by mixing the sample with potassium bromide, ensuring adequate transparency for infrared analysis. X-ray diffraction (XRD) patterns were performed at room temperature with a Rigaku Mini-flex powder diffractometer (Rigaku Corporation, Tokyo, Japan), with Cu-K $\alpha$  radiation ( $\lambda = 1.5418 \text{ \AA}$ ) and with the tube operating at 40 kV and 15 mA in continuous mode with a sweep rate of 0.02° at a speed of 10°/min.

### Electrochemical measurement

The electrochemical performance of the samples  $Ti_3C_2T_x$  and  $Ti_3C_2T_x$ -Alg was evaluated using an Autolab PGSTAT 302N potentiostat/galvanostat (Metrohm, Switzerland) in a two-electrode configuration. Cyclic voltammetry (CV) was conducted across various scan rates (5 mVs<sup>-1</sup> to 400 mVs<sup>-1</sup>). Electrochemical impedance spectroscopy (EIS) measurements

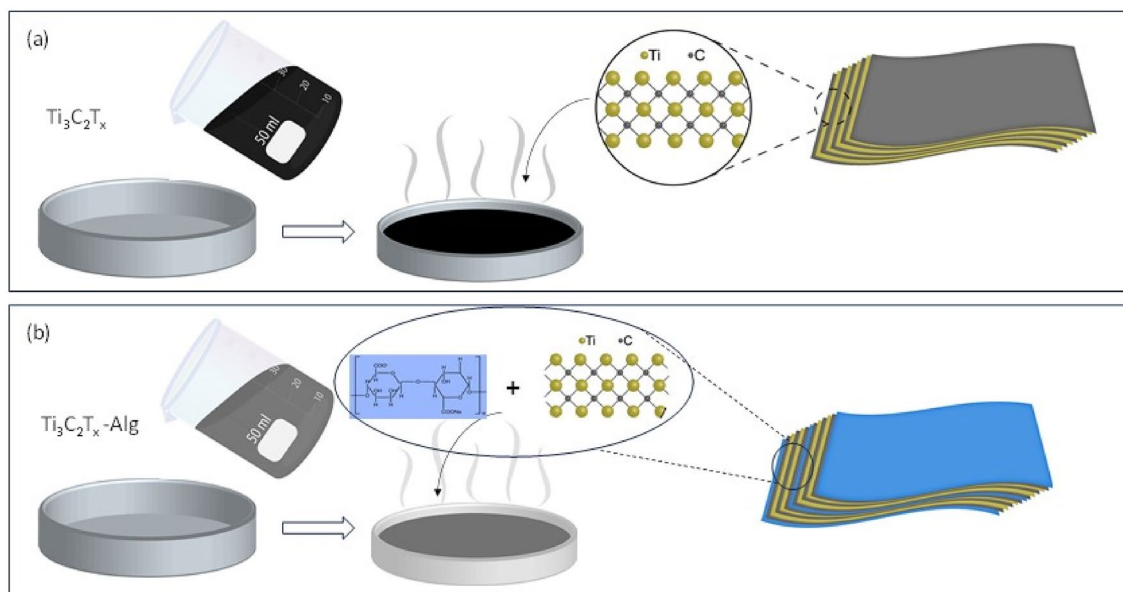


**Figure 9:** Scheme for the preparation of (a)  $\text{Ti}_3\text{C}_2\text{T}_x$  films following the step of increasing concentration by centrifuging it at 8000 rpm for 10 min with the formation of a film from evaporation of the solvent based on a drop-cast procedure and (b)  $\text{Ti}_3\text{C}_2\text{T}_x$ -Alg films prepared according to the previous step with the incorporation of alginate into the drop-cast step.

were acquired over a frequency range of 0.01 Hz to 1 MHz, applying an AC voltage of 10 mV with 200-mV external bias. The specific capacitances were determined based on the mass and geometric area. The electrode areal capacitance ( $C_{AeCV}$ ) as a function of the scan rate was calculated from the area enclosed by the CV curves, as described by Eq. 2, with the electrode gravimetric capacitance ( $C_{GeCV}$ ) was obtained using Eq. 3 [28, 69–71].

$$C_{AeCV} = \frac{\int i dV}{v \cdot A \cdot \Delta V}, \quad (2)$$

$$C_{GeCV} = \frac{2 \cdot \int i dV}{v \cdot m \cdot \Delta V} \quad (3)$$

In Eqs. 2 and 3,  $i$  is the current (in A),  $V$  is the applied potential (in V),  $v$  is the scan rate (V/s),  $A$  is the electrode area (in  $\text{cm}^2$ ),  $m$  is the mass of the active material (in grams), and  $\Delta V$  is the potential window (in volts). The factor of 2 accounts for both the charge and discharge processes in the CV cycle, as a complete cycle involves contributions from both phases. For a symmetric assembly of two-electrode supercapacitors, the system can be modeled as two identical single-electrode capacitors arranged in series. As a result, the total capacitance is effectively divided equally between the two electrodes. Under this configuration, the mass of one electrode corresponds to half of the system's total mass. In contrast, the geometric area of a single electrode is equivalent to the total electrode area [51, 72]. Correspondingly, galvanostatic charge–discharge (GCD) measurements were also used

to calculate the specific capacitance of devices, according to Eqs. 4 and 5 [51, 57, 72].

$$C_{AGCD} = \frac{2 \cdot i \cdot \Delta t}{A \cdot V}, \quad (4)$$

$$C_{GCD} = \frac{4 \cdot i \cdot \Delta t}{m \cdot V}. \quad (5)$$

In Eqs. 4 and 5,  $i$  is the discharge current (in amperes),  $\Delta t$  is the time from the beginning until the complete discharge of the device (in seconds),  $A$  is the electrode area (in  $\text{cm}^2$ ),  $m$  is the mass of the active material (in grams), and  $V$  is the voltage difference below the IR drop until zero (complete discharge) [73]. These GCD experiments were performed at various current densities (from 1.1 A/g to 2.2 A/g).

## Acknowledgments

M.H.M.F. thanks the financial support from FAPESP (2024/13749-4) and CNPq (173177/2024-7). H.P.O. thanks the financial support from CNPq (303997/2021-4), FINEP, FACEPE, INCT-INFO (National Institute of Photonics), and the Coordenação de Aperfeiçoamento de Pessoal de Nível Superior – Brasil (CAPES) – Finance Code 001. E.C. also acknowledges CNPq grants' support (409215/2022-8 and 308835/2019-0). H.S. Barud thanks (CEMASU) FAPESP-Funding (Process: 2021/11965-3) and (Process: 2017/50334-3), the National Council of Scientific and Technological Development/CNPq (Grant: 309614/2021-0), National Institutes of Science and Technology (INCTs), INCT

Polysaccharides (Grant: 406973/2022-9), INCT Circularity in Polymer Materials (grant no. 406925/2022-4), and INCT-INFO (National Institute of Photonics).

### Author contributions

Jorge Alexandre Alencar Fotius contributed to conceptualization, methodology, investigation, formal analysis, and writing—original draft; Murilo Henrique Moreira Facure contributed to conceptualization, methodology, investigation, formal analysis, and writing—reviewing and editing; Daniel Souza Correa contributed to investigation, resources, supervision, formal analysis, and writing—reviewing and editing; Emanuel Carrilho contributed to investigation, resources, supervision, formal analysis, and writing—reviewing and editing; Hernane da Silva Barud contributed to investigation, resources, supervision, formal analysis, and writing—reviewing and editing; Helinando Pequeno de Oliveira contributed to conceptualization, methodology, investigation, formal analysis, resources, supervision, and writing—reviewing and editing.

### Funding

Brazilian Funding Agencies FACEPE, FAPESP, CAPES, FINEP, National Institutes of Science and Technology (INCTs), and CNPq.

### Data availability

Data will be made available on reasonable request.

### Declarations

**Conflict of interest** On behalf of all authors, the corresponding author states that there is no conflict of interest.

### References

1. S.N.K. Pavithra, S.M. Jeong, C.S. Rout, MXene-carbon based hybrid materials for supercapacitor applications. *Energy Adv.* **3**(2), 341 (2024)
2. W.S. Poh, W.J. Yiang, W.-J. Ong, P.L. Show, C.Y. Foo, Enhancing MXene-based supercapacitors: role of synthesis and 3D architectures. *J. Energy Chem.* **91**, 1 (2024)
3. J.J. Alcaraz-Espinoza, H.P. de Oliveira, Flexible supercapacitors based on a ternary composite of polyaniline/polypyrrole/graphite on gold coated sandpaper. *Electrochim. Acta* **274**, 200 (2018)
4. H.P. De Oliveira, S.A. Sydlik, T.M. Swager, Supercapacitors from free-standing polypyrrole/graphene nanocomposites. *J. Phys. Chem. C* **117**(20), 10270 (2013)
5. A.H.P. De Oliveira, H.P. De Oliveira, Carbon nanotube/polypyrrole nanofibers core-shell composites decorated with titanium dioxide nanoparticles for supercapacitor electrodes. *J. Power. Sources* **268**, 45 (2014)
6. M. Pathak, P. Mane, B. Chakraborty, C.S. Rout, Facile in-situ grown spinel MnCo<sub>2</sub>O<sub>4</sub>/MWCNT and MnCo<sub>2</sub>O<sub>4</sub>/Ti<sub>3</sub>C<sub>2</sub> MXene composites for high-performance asymmetric supercapacitor with theoretical insight. *J. Energy Storage* **66**, 107475 (2023)
7. Y. Ibrahim, A. Mohamed, A.M. Abdelgawad, K. Eid, A.M. Abdullah, A. Elzatahry, The recent advances in the mechanical properties of self-standing two-dimensional MXene-based nanostructures: deep insights into the supercapacitor. *Nano-materials* **10**(10), 1916 (2020)
8. Z. Bao, C. Lu, X. Cao, P. Zhang, L. Yang, H. Zhang, D. Sha, W. He, W. Zhang, L. Pan, Z. Sun, Role of MXene surface terminations in electrochemical energy storage: a review. *Chinese Chem. Lett.* **32**(9), 2648 (2021)
9. N. Khosroshahi, M. Bakhtian, A. Asadi, V. Safarifard, Revolutionizing energy storage: the emergence of MOF/MXene composites as promising supercapacitors. *Nano Express* **4**(4), 042002 (2023)
10. N. Kitchamsetti, J.S. Cho, A roadmap of recent advances in MXene@MOF hybrids, its derived composites: synthesis, properties, and their utilization as an electrode for supercapacitors, rechargeable batteries and electrocatalysis. *J. Energy Storage* **80**, 110293 (2024)
11. Y. Dong, D. Sang, C. He, X. Sheng, L. Lei, Mxene/alginate composites for lead and copper ion removal from aqueous solutions. *RSC Adv.* **9**(50), 29015 (2019)
12. Y. Wang, W. Zhang, Y. Shan, X. Yu, K. Chen, Preparation of polyacrylamide/calcium alginate@Ti<sub>3</sub>C<sub>2</sub>Tx composite hydrogels with high adhesive performance for flexible supercapacitor electrolytes. *Colloids Surfaces A Physicochem. Eng. Asp.* **666**, 131312 (2023)
13. L. Cheng, R. Tian, Y. Zhao, Z. Wei, X. Pu, Y.L. Zhu, D. Zhang, F. Du, Small things make a big difference: conductive cross-linking sodium Alginate@MXene binder enables high-volumetric-capacity and high-mass-loading Li-S battery. *Nano Lett.* **23**(22), 10538 (2023)
14. P. Zhang, J. Li, D. Yang, R.A. Soomro, B. Xu, Flexible carbon dots-intercalated MXene film electrode with outstanding volumetric performance for supercapacitors. *Adv. Funct. Mater.* (2023). <https://doi.org/10.1002/adfm.202209918>
15. Z. Qin, X. Chen, Y. Lv, B. Zhao, X. Fang, K. Pan, Wearable and high-performance piezoresistive sensor based on nanofiber/sodium alginate synergistically enhanced MXene composite aerogel. *Chem. Eng. J.* **451**, 138586 (2023)
16. B. Wicklein, G. Valurouthu, H. Yoon, H. Yoo, S. Ponnann, M. Mahato, J. Kim, S.S. Ali, J.Y. Park, Y. Gogotsi, I.-K. Oh, Influence of MXene composition on triboelectricity of

- MXene-Alginate nanocomposites. *ACS Appl. Mater. Interfaces* Acsami. (2024). <https://doi.org/10.1021/acsami.4c03298>
17. C. Zhao, B. Xia, A. Hu, M. Hou, T. Li, S. Wang, M. Chen, W. Dong, Preparation of high electromagnetic interference shielding and humidity responsivity composite film through modified Ti<sub>3</sub>C<sub>2</sub>T<sub>x</sub> MXene cross-linking with sodium alginate. *Int. J. Biol. Macromol.* **236**, 123939 (2023)
  18. G. Zhao, C. Sui, L. Miao, J. Li, L. Wen, G. Cheng, C. Zhao, W. Hao, Y. Sang, J. Li, Z. Zhang, Y. Zhao, F. Wang, R. Liu, X. He, C. Wang, Strong and continuous MXene/sodium alginate composite fibers prepared by immersion rotary jet spinning process with outstanding electromagnetic interference shielding performance. *Chem. Eng. J.* **469**, 143983 (2023)
  19. X. Ye, Y. Ma, Z. Tian, H. Sun, Z. Zhu, J. Li, W. Liang, A. Li, Shape-stable MXene/sodium alginate/carbon nanotubes hybrid phase change material composites for efficient solar energy conversion and storage. *Compos. Sci. Technol.* **230**, 109794 (2022)
  20. H. Zhu, W. Dai, L. Wang, C. Yao, C. Wang, B. Gu, D. Li, J. He, Electroactive oxidized Alginate/Gelatin/MXene (Ti<sub>3</sub>C<sub>2</sub>T<sub>x</sub>) composite hydrogel with improved biocompatibility and self-healing property. *Polymers (Basel)* **14**(18), 3908 (2022)
  21. Y. Hu, Q. Zeng, Y. Hu, J. He, H. Wang, C. Deng, D. Li, MXene/zinc ion embedded agar/sodium alginate hydrogel for rapid and efficient sterilization with photothermal and chemical synergetic therapy. *Talanta* **266**, 125101 (2024)
  22. Z. Liang, Z. Sang, Y. Li, Z. Chen, X. Mei, X. Ren, Enhancing the performance of injectable self-activating PVA-alginate hydrogel by Ag@MXene nanozyme as NIR responsive and photoenhanced antibacterial platform for wound healing. *Carbohydr. Polym.* **357**, 123434 (2025)
  23. S.D. Sutar, A. Swami, A Ti<sub>3</sub>C<sub>2</sub>T<sub>x</sub> MXene/alginate acid-derived mesoporous carbon nanocomposite as a potential electrode material for coin-cell asymmetric supercapacitors. *Nanoscale* **17**(8), 4750 (2025)
  24. H. Alnoor, A. Elbukova, J. Palisaitis, I. Persson, E.N. Tseng, J. Lu, L. Hultman, P.O.Å. Persson, Exploring MXenes and their MAX phase precursors by electron microscopy. *Mater. Today Adv.* **9**, 100123 (2021)
  25. Y. Jin, Y. Fan, X. Meng, W. Zhang, B. Meng, N. Yang, S. Liu, Theoretical and experimental insights into the mechanism for gas separation through nanochannels in 2D laminar MXene membranes. *Processes* **7**(10), 751 (2019)
  26. B.S. Shen, H. Wang, L.J. Wu, R.S. Guo, Q. Huang, X.B. Yan, All-solid-state flexible microsupercapacitor based on two-dimensional titanium carbide. *Chinese Chem. Lett.* **27**(10), 1586 (2016)
  27. X. Zhang, L. Qian, H. Yang, Z. Chen, L. Yao, Z. Chen, Effect of electron beam irradiation on the properties of MXene film. *J. Mater. Sci. Mater. Electron.* **34**(17), 1362 (2023)
  28. D. Spurling, H. Krüger, N. Kohlmann, F. Rasch, M.P. Kremer, L. Kienle, R. Adelung, V. Nicolosi, F. Schütt, 3D networked MXene thin films for high performance supercapacitors. *Energy Storage Mater.* **65**, 103148 (2024)
  29. P. Tetiana, Z. Danzhen, B. David, S. Kateryna, D. Marley, V. Geetha, I. Alex, C. Benjamin, Z. Teng, Fourier-transform infrared spectral library of MXenes. *Chem. Mater.* **36**, 8437 (2024)
  30. Y.-Z. Yan, S. Li, S.S. Park, W.-J. Zhang, J.S. Lee, J.R. Kim, D.G. Seong, C.-S. Ha, "One stone, two birds" solvent system to fabricate microcrystalline cellulose-Ti<sub>3</sub>C<sub>2</sub>T<sub>x</sub> nanocomposite film as a flexible dielectric and thermally conductive material. *Nano Res.* **16**(2), 3240 (2023)
  31. S.G.M. Ivana, S.M. Ivan, S. Zorica, Preparation and characterization of alginate hydrogels with high water-retaining capacity. *Polymers (Basel)* **15**, 2592 (2023)
  32. Y. Xie, X. Xiong, K. Han, Organic molecule intercalated multi-layer Ti<sub>3</sub>C<sub>2</sub>T<sub>x</sub> MXene with enhanced electrochemical lithium and sodium storage. *Ionics (Kiel)* **27**(8), 3373 (2021)
  33. M. Kurtoglu, M. Naguib, Y. Gogotsi, M.W. Barsoum, First principles study of two-dimensional early transition metal carbides. *MRS Commun.* **2**(4), 133 (2012)
  34. M. Naguib, M. Kurtoglu, V. Presser, J. Lu, J. Niu, M. Heon, L. Hultman, Y. Gogotsi, M.W. Barsoum, Two-dimensional nanocrystals produced by exfoliation of Ti<sub>3</sub>AlC<sub>2</sub>. *Adv. Mater.* **23**(37), 4248 (2011)
  35. M. Alhabeab, K. Maleski, B. Anasori, P. Lelyukh, L. Clark, S. Sin, Y. Gogotsi, Guidelines for synthesis and processing of two-dimensional titanium carbide (Ti<sub>3</sub>C<sub>2</sub>T<sub>x</sub> MXene). *Chem. Mater.* **29**(18), 7633 (2017)
  36. O. Mashtalir, M. Naguib, V.N. Mochalin, Y. Dall'Agnese, M. Heon, M.W. Barsoum, Y. Gogotsi, Intercalation and delamination of layered carbides and carbonitrides. *Nat. Commun.* **4**(1), 1716 (2013)
  37. F. Shahzad, M. Alhabeab, C.B. Hatter, B. Anasori, S. Man Hong, C.M. Koo, Y. Gogotsi, Electromagnetic interference shielding with 2D transition metal carbides (MXenes). *Science* **353**(6304), 1137 (2016)
  38. Z. Ling, C.E. Ren, M.-Q. Zhao, J. Yang, J.M. Giammarco, J. Qiu, M.W. Barsoum, Y. Gogotsi, Flexible and conductive MXene films and nanocomposites with high capacitance. *Proc. Natl. Acad. Sci.* **111**(47), 16676 (2014)
  39. G. Leftheriotis, S. Papaefthimiou, P. Yianoulis, Dependence of the estimated diffusion coefficient of Li<sub>x</sub>WO<sub>3</sub> films on the scan rate of cyclic voltammetry experiments. *Solid State Ion.* **178**(3-4), 259 (2007)
  40. M. Arun Prasad, M.V. Sangaranarayanan, Analysis of the diffusion layer thickness, equivalent circuit and conductance behaviour for reversible electron transfer processes in linear sweep voltammetry. *Electrochim. Acta* **49**(3), 445 (2004)
  41. R.M.A.P. Lima, H.P. de Oliveira, Carbon dots reinforced polypyrrole/graphene nanoplatelets on flexible eggshell membranes as electrodes of all-solid flexible supercapacitors. *J. Energy Storage* **28**, 101284 (2020)

42. M. Forghani, S.W. Donne, Method comparison for deconvoluting capacitive and pseudo-capacitive contributions to electrochemical capacitor electrode behavior. *J. Electrochem. Soc.* **165**(3), A664 (2018)
43. L.M. Da Silva, L.G. De Sousa, R. Vicentini, J.P. Aguiar, G. Doubek, H. Zanin, Proposal of a novel methodology for the electrochemical characterization of well-behaved redox-active materials used in supercapacitors. *Electrochim. Acta* **457**, 142458 (2023)
44. V. Augustyn, P. Simon, B. Dunn, Pseudocapacitive oxide materials for high-rate electrochemical energy storage. *Energy Environ. Sci.* **7**(5), 1597 (2014)
45. S. Peretz, D.F. Anghel, E. Vasilescu, M. Florea-Spiroiu, C. Stoian, G. Zgherea, Synthesis, characterization and adsorption properties of alginate porous beads. *Polym. Bull.* **72**(12), 3169 (2015)
46. J. Sun, H. Tan, Alginate-based biomaterials for regenerative medicine applications. *Materials (Basel)* **6**(4), 1285 (2013)
47. H. Zhang, C. Hao, T. Fu, D. Yu, J. Howe, K. Chen, N. Yan, H. Ren, H. Zhai, Gradient-layered MXene/Hollow lignin nanospheres architecture design for flexible and stretchable supercapacitors. *Nano-Micro Lett.* **17**(1), 43 (2025)
48. D.H.E. Darling, Conductivity of sulfuric acid solutions. *J. Chem. Eng. Data* **9**, 421 (1964)
49. J. Fu, L. Li, D. Lee, J.M. Yun, B.K. Ryu, K.H. Kim, Enhanced electrochemical performance of Ti<sub>3</sub>C<sub>2</sub>T MXene film based supercapacitors in H<sub>2</sub>SO<sub>4</sub>/KI redox additive electrolyte. *Appl. Surf. Sci.* **504**, 144250 (2020)
50. X. Hui, X. Ge, R. Zhao, Z. Li, L. Yin, Interface chemistry on MXene-based materials for enhanced energy storage and conversion performance. *Adv. Funct. Mater.* **30**(50), 2005190 (2020)
51. Y. Shao, M.F. El-Kady, C. Lin, G. Zhu, K.L. Marsh, J.Y. Hwang, Q. Zhang, Y. Li, H. Wang, R.B. Kaner, 3D freeze-casting of cellular graphene films for ultrahigh-power-density supercapacitors. *Adv. Mater.* **28**(31), 6719 (2016)
52. S. Ortaboy, J.P. Alper, F. Rossi, G. Bertoni, G. Salviati, C. Carraro, R. Maboudian, MnO<sub>x</sub>-decorated carbonized porous silicon nanowire electrodes for high performance supercapacitors. *Energy Environ. Sci.* **10**(6), 1505 (2017)
53. J. Tian, Z. Sun, C. Shi, Z. Huang, Rapid fabrication of tough sodium alginate/MXene/poly(vinyl alcohol) dual-network hydrogel electrolytes for flexible all-solid-state supercapacitors. *Int. J. Biol. Macromol.* **248**, 125937 (2023)
54. Z. Lin, D. Barbara, P.-L. Taberna, K.L. Van Aken, B. Anasori, Y. Gogotsi, P. Simon, Capacitance of Ti<sub>3</sub>C<sub>2</sub>T<sub>x</sub> MXene in ionic liquid electrolyte. *J. Power. Sources* **326**, 575 (2016)
55. H. Chen, L. Yu, Z. Lin, Q. Zhu, P. Zhang, N. Qiao, B. Xu, Carbon nanotubes enhance flexible MXene films for high-rate supercapacitors. *J. Mater. Sci.* **55**(3), 1148 (2020)
56. Z. He, L. Yao, W. Guo, N. Sun, F. Wang, Y. Wang, R. Wang, F. Wang, pseudocapacitance of bimetallic solid-solution MXene for supercapacitors with enhanced electrochemical energy storage. *Adv. Funct. Mater.* **33**(52), 2305251 (2023)
57. A. Mateen, M.Z. Ansari, Q. Abbas, A. Muneeb, A. Hussain, E.T. Eldin, F.M. Alzahrani, N.S. Alsaiani, S. Ali, M.S. Javed, In situ nitrogen functionalization of 2D-Ti<sub>3</sub>C<sub>2</sub>T<sub>x</sub>-MXenes for high-performance Zn-ion supercapacitor. *Molecules* **27**(21), 7446 (2022)
58. W. Luo, Y. Wei, Z. Zhuang, Z. Lin, X. Li, C. Hou, T. Li, Y. Ma, Fabrication of Ti<sub>3</sub>C<sub>2</sub>T<sub>x</sub> MXene/polyaniline composite films with adjustable thickness for high-performance flexible all-solid-state symmetric supercapacitors. *Electrochim. Acta* **406**, 139871 (2022)
59. Q.X. Xia, N.M. Shinde, J.M. Yun, T. Zhang, R.S. Mane, S. Mathur, K.H. Kim, Bismuth Oxychloride/MXene symmetric supercapacitor with high volumetric energy density. *Electrochim. Acta* **271**, 351 (2018)
60. R. Zhang, J. Dong, W. Zhang, L. Ma, Z. Jiang, J. Wang, Y. Huang, Synergistically coupling of 3D FeNi-LDH arrays with Ti<sub>3</sub>C<sub>2</sub>T<sub>x</sub>-MXene nanosheets toward superior symmetric supercapacitor. *Nano Energy* **91**, 106633 (2022)
61. J. Fu, L. Li, J.M. Yun, D. Lee, B.K. Ryu, K.H. Kim, Two-dimensional titanium carbide (MXene)-wrapped sisal-Like NiCo<sub>2</sub>S<sub>4</sub> as positive electrode for High-performance hybrid pouch-type asymmetric supercapacitor. *Chem. Eng. J.* **375**, 121939 (2019)
62. X. Li, J. Hao, R. Liu, H. He, Y. Wang, G. Liang, Y. Liu, G. Yuan, Z. Guo, Interfacing MXene flakes on fiber fabric as an ultrafast electron transport layer for high performance textile electrodes. *Energy Storage Mater.* **33**, 62 (2020)
63. A. Akilli, B.H. Taymaz, V. Eskizeybek, H. Kaniş, Enhanced performance of MXene-based supercapacitor via new activated carbon-nafion composite cathode. *J. Phys. Chem. Solids* **199**, 112523 (2025)
64. E. Baasanjav, K.A.S. Raj, H. Hakkeem, C.S. Rout, S.M. Jeong, High-performance asymmetric supercapacitors based on 2D MXene/NiCoP hybrid and ZIF derived porous nanocarbon. *J. Mater. Sci. Technol.* **228**, 42 (2025)
65. Y. Liao, X. Bin, J. Xu, X. He, W. Que, Nitrogen-doped mxene electrodes for high-voltage window supercapacitors in organic electrolytes. *Chemistry (Easton)* **7**(1), 13 (2025)
66. T. He, X. Li, B. Sun, L. Lin, F. Guo, G. Diaoy, Y. Piao, W. Zhang, Preparation of cyclodextrin polymer-functionalized polyaniline/MXene composites for high-performance supercapacitor. *RSC Adv.* **14**(19), 13685 (2024)
67. Z. Li, J. Li, B. Wu, H. Wei, H. Guo, Z.M. El-Bahy, B. Liu, M. He, S. Melhi, X. Shi, S.D. Mekkey, Y. Sun, B. Bin Xu, Z. Guo, Interfacial-engineered robust and high performance flexible polylactic acid/polyaniline/MXene electrodes for high-performance supercapacitors. *J. Mater. Sci. Technol.* **203**, 201 (2024)

68. M.H.M. Facure, K. Matthews, R. Wang, R.W. Lord, D.S. Correa, Y. Gogotsi, Pillaring effect of nanodiamonds and expanded voltage window of Ti<sub>3</sub>C<sub>2</sub>T<sub>x</sub> supercapacitors in AlCl<sub>3</sub> electrolyte. *Energy Storage Mater.* **61**(August), 102919 (2023)
69. Y. Ji, Y. You, G. Xu, X. Yang, Y. Liu, Engineering metal organic framework (MOF)@MXene based electrodes for hybrid supercapacitors – a review. *Chem. Eng. J.* **483**, 149365 (2024)
70. D.M. Sayed, M.M. Taha, L.G. Ghanem, M.S. El-Deab, N.K. Allam, Hybrid supercapacitors: a simple electrochemical approach to determine optimum potential window and charge balance. *J. Power. Sources* **480**, 229152 (2020)
71. T.S. Mathis, N. Kurra, X. Wang, D. Pinto, P. Simon, Y. Gogotsi, Energy storage data reporting in perspective—guidelines for interpreting the performance of electrochemical energy storage systems. *Adv. Energy Mater.* **9**(39), 1902007 (2019)
72. M.Z. Iqbal, U. Aziz, Supercapattery: merging of battery-supercapacitor electrodes for hybrid energy storage devices. *J. Energy Storage* **46**, 103823 (2022)
73. S. Roldán, D. Barreda, M. Granda, R. Menéndez, R. Santamaría, C. Blanco, An approach to classification and capacitance expressions in electrochemical capacitors technology. *Phys. Chem. Chem. Phys.* **17**(2), 1084 (2015)

**Publisher's Note** Springer Nature remains neutral with regard to jurisdictional claims in published maps and institutional affiliations.

Springer Nature or its licensor (e.g. a society or other partner) holds exclusive rights to this article under a publishing agreement with the author(s) or other rightsholder(s); author self-archiving of the accepted manuscript version of this article is solely governed by the terms of such publishing agreement and applicable law.